



Deep learning for automatic assessment of breathing-debonds in stiffened composite panels using non-linear guided wave signals

Shirsendu Sikdar^{a,*}, Wiesław Ostachowicz^b, Abhishek Kundu^a

^a Cardiff School of Engineering, Cardiff University, The Parade, Queen's Building, Cardiff, CF24 3AA, UK

^b Institute of Fluid-Flow Machinery, Polish Academy of Sciences, 14, Fiszerza Street, Gdansk 80-231, Poland

ARTICLE INFO

Keywords:

Nonlinear guided waves
Stiffened composite structure
Breathing-debond
Deep learning
Structural health monitoring

ABSTRACT

This paper presents a new structural health monitoring strategy based on a deep learning architecture that uses nonlinear ultrasonic signals for the automatic assessment of breathing-like debonds in lightweight stiffened composite panels (SCPs). Towards this, nonlinear finite element simulations of ultrasonic guided wave (GW) response of SCPs and laboratory-based experiments have been undertaken on multiple composite panels with and without baseplate-stiffener debonds using fixed a network of piezoelectric transducers (actuators/sensors). GW signals in the time domain are collected from the network of sensors onboard the SCPs and these signals in the frequency domain represent nonlinear signatures as the existence of higher harmonics. These higher harmonic signals are separated from the GWs (raw) and converted to images of time–frequency scalograms using continuous wavelet transforms. A deep learning architecture is designed that uses the convolutional neural network to automatically extract the discrete image features for the characterization of SCP under healthy and variable breathing-debond conditions. The proposed deep learning-aided health monitoring strategy demonstrates a promising autonomous inspection potential with high accuracy for such complex structures subjected to multi-level breathing-debond regions.

1. Introduction

Lightweight fibre-reinforced composites have gained popularity in aeronautic, aerospace, marine, infrastructure and automobile engineering sectors, owing to their high stiffness/weight ratio, fire resistance and acoustic damping, amongst others [1–5]. Stiffened composites are often used for the lightweight construction of these engineering structures [6,7]. Various types of stiffeners (e.g., cross-sections of I, L, T) are bonded to the base plate of these structures. At these stiffener-baseplate bond interphase, breathing type debond can occur owing to cyclic loading, improper handling, impact and ageing [8,9]. While in service, these debond can grow further and lead to a catastrophic structural failure, if not identified beforehand [10,11]. Hence, detecting and characterising these hidden damages in stiffened composites is important.

In [12–15], it was shown that the structural health monitoring (SHM) methods based on guided wave (GW) propagation have the potential for the accurate detection of hidden defects in complex composites with multiple layers. Such linear and nonlinear GW propagation-based SHM techniques offer long-range monitoring with high sensitivity

against minor defects/discontinuities in layers [16–19]. These SHM methods often involve the application of lightweight and economic broadband transducers such as the network of surface-mounted piezoelectric lead zirconium titanate transducers (PZTs) [14,15].

The breathing debonds in composites are complex and often difficult to identify using trad SHM methods [20,21]. This breathing-type debond can sometimes behave as open (i.e. debond) or closed (i.e. undamaged) regions, owing to the occurrence of ‘breathing behaviour’ under dynamic wave loading [21,22]. The breathing phenomenon of such debonds generates nonlinear ultrasonic waves that involve higher harmonics [23,24], sub-harmonics [25], mixed frequency–response [26], and non-linear resonance [27]. Several studies [24,28,29] have demonstrated that the nonlinear response features are responsive to contact-type damage (e.g., breathing crack, kissing-delamination) and are not much influenced by operational conditions. Many authors [30,31] have analysed the generation of higher-harmonics, due to the occurrence of contact nonlinearity (often occurring for breathing-type damage) in the structures. In [23], contact-acoustic non-linearity (CAN) that occurs owing to the breathing-type cracks was investigated using signals from a PZT network. Nonlinear elastic wave signal-based

* Corresponding author.

E-mail address: SikdarS@cardiff.ac.uk (S. Sikdar).

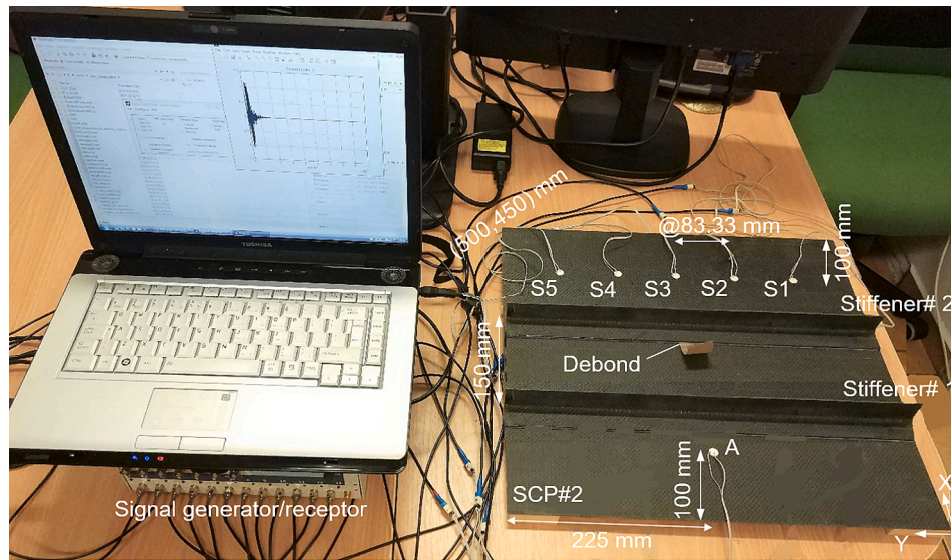


Fig. 1. Experimental setup: PZT-induced ultrasonic GW propagation in SCPs.

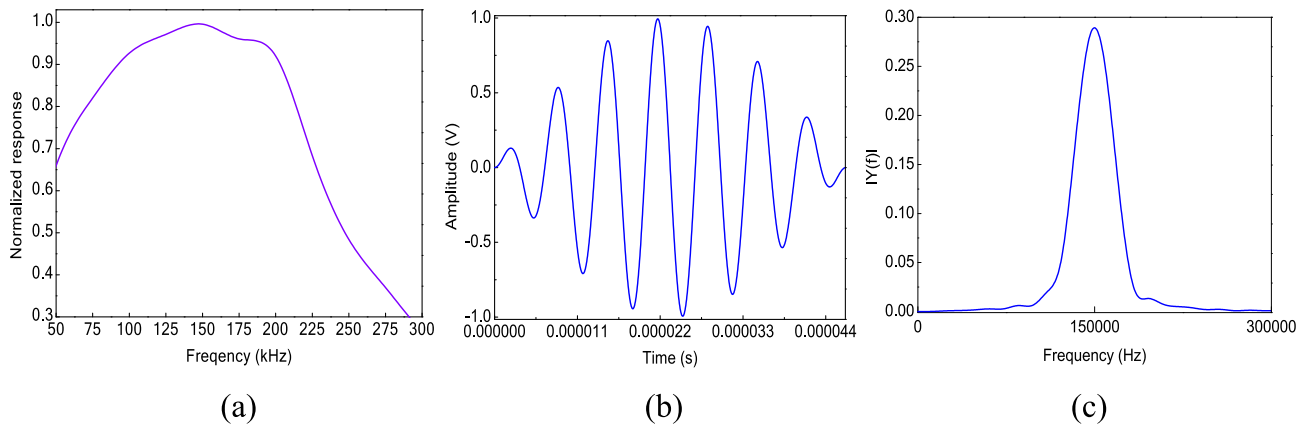


Fig. 2. (a) Frequency modulation curve, (b) selected actuation signal and (c) its FFT.

SHM techniques are also presented by some other researchers [32,33].

In recent times, structural response data-based machine learning approaches are gaining popularity for autonomous condition monitoring of structures [34–38]. Deep learning algorithms using Convolutional Neural Network (CNN) have demonstrated their capability in the image-based characterization of structural conditions [34,35]. The CNN algorithm can effectively handle the grid-like inputs from images to generate similar image features from the local regions of alike patterns [34,39]. Image-based deep learning involves large datasets that can be produced synthetically by adding different levels of noise (e.g., Gaussian zero mean noise) to the actual images, which is known as ‘data augmentation’ [40–42]. Recent studies [42,43] have presented deep learning based SHM methods for autonomous assessment of static damage/delamination in laminated composites. The literature review revealed that no investigation has been undertaken in the area of identification of breathing-type damage-induced nonlinear ultrasonic wave features using an automated deep learning approach. This paper aims to address this important research gap with a deep learning-based SHM strategy.

A CNN-based SHM strategy is presented in this paper for the automatic characterization of carbon fibre-reinforced stiffened composite panels (SCPs) with and without baseplate-stiffener debond using the raw GW signals and the filtered time-domain higher-harmonic signals. A series of laboratory experiments and numerical finite element based

numerical simulations have been carried through on multiple SCP samples. The numerical and experimental GW signals are translated to images of RGB (red, green, blue) scalograms (time–frequency) using the Continuous Wavelet Transform (CWT). These scalograms have been supplied as input to the designed deep learning architecture to perform the training/validation/testing operations. This paper is structured as follows. Section 2 presents the details of laboratory experiments on SCP samples for SCPs with breathing debonds. In Section 3 the details of finite element modeling for nonlinear numerical simulations of GW propagation in SCP are described. Section 4 describes the details of the deep learning architecture for SHM of SCPs. The experimental results, findings, and discussions around them are presented in Section 5. The main conclusions from this study and scope of future research in this area are detailed in Section 6.

2. Experimental procedure

A series of ultrasonic GW-based experiments are conducted in the laboratory on.

- (i) an undamaged (healthy) SCP- marked as ‘UD’,
- (ii) an SCP with a baseplate-stiffener 2 debond- marked as ‘DSt2’
- (iii) an SCP with a baseplate-stiffener 1 debond- marked as ‘DSt1’.

Table 1
Material properties of the CFCL.

Material	E_{11} (GPa)	E_{22} (GPa)	E_{33} (GPa)	G_{12} (GPa)	G_{13} (GPa)	G_{23} (GPa)	ν_{12}	ν_{13}	ν_{23}	ρ (kg/m ³)
CFCL	77.46	77.46	11.24	4.15	3.625	3.625	0.03	0.37	0.37	1655

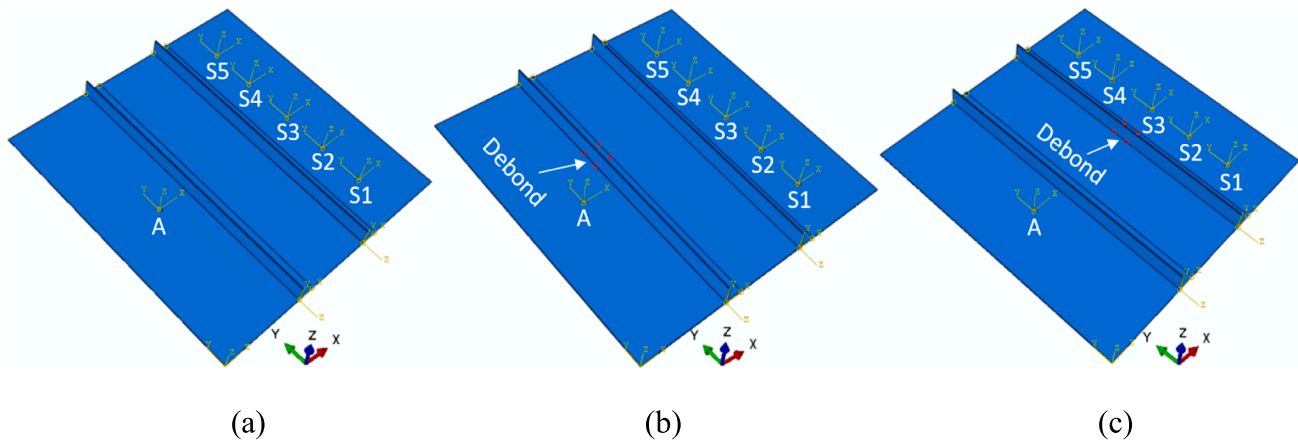


Fig. 3. Numerical models of the experimental SCPs corresponding to (a) undamaged case, (b) DSt2 case and (c) DSt1 case.

In the SCP samples, two 450.00 mm long L shaped (30.00×30.00 mm) stiffeners are attached to the base plate ($500.00 \times 450.00 \times 2.00$ mm) using the epoxy resin adhesive. At the stiffener-baseplate interface, artificial debonds ($30.00 \text{ mm} \times 30.00 \text{ mm}$) are induced by placing 0.05 mm thin Teflon films while manufacturing the samples (ii) and (iii). A bonded PZT (thickness = 0.05 mm, diameter = 10 mm) network is mounted on the SCP's top surface for the actuation and reception of ultrasonic signals. A signal generation/acquisition system (sampling rate: 1 M sample/s) was utilized to control the PZTs (Fig. 1). These SCP samples are made of 2.00 mm thick quasi-isotropic (lay-up $[0/90/+45/-45]_S$) laminates of carbon-fibre (CFCL). The prepreg lay-up process is used for manufacturing the CFCL with the following material properties:

- Carbon-fibre: volume-fraction of fibre = 0.565, mass density (ρ) = 1650 kg/m³, Poisson's ratio (ν) = 0.25, Elastic modulus (E) = 257.5 GPa.
- Matrix: $E = 3.45$ GPa, $\rho = 1270$ kg/m³ and $\nu = 0.35$.
- Epoxy resin: $E = 3.0$ GPa, $\rho = 1150$ kg/m³ and $\nu = 0.34$.

Fig. 1 shows the laboratory-based setup for the SCP sample with DSt2 debond, the PZT network of 5 sensors: S1, S2, S3, S4, S5 and an actuator: 'A'. The excitation signal was selected based on trials for a range of carrier frequencies and cycles. In the process, the 7-cycle tone-burst sine signal produced the most prominent higher harmonics in the frequency domain. A suitable actuation frequency was identified by actuating a series of sine waves of 7-cycle with different carrier frequencies through the actuator 'A', and the propagated signals are collected at the sensor 'S3' (ref. Fig. 1). Thus, a frequency-response plot was generated as shown in Fig. 2(a). The plot shows higher magnitudes of response around 150 kHz. Thus, a Hanning window modulated 7-cycle 150 kHz sine pulse as shown in Fig. 2(b) is selected as the excitation signal for the experiments and simulations. Fig. 2(c) represents a Fast Fourier transform (FFT) of the actuator signal in the frequency domain. The actuator PZT introduces the excitation (Fig. 2(a)) and generates the GW propagation in the SCP. These GWs are registered at each of the PZT sensors (S1, S2, S3, S4 and S5) in the network.

3. Finite element modeling

The numerical simulation models are validated for all 3 experimental (baseline) cases and then extended for different debond locations and variable actuation positions to generate a large dataset for the deep learning model. As the experiments could be conducted only for (i) a UD, (ii) an SCP with a DSt2 debond and (iii) an SCP with a DSt1 debond. 3D nonlinear simulation of ultrasonic GW propagation in SCPs with contact-acoustic-nonlinearity owing to the breathing-debond phenomenon is challenging. In this study, finite element simulation of GW propagation in SCP samples ($450 \times 450 \times 1$ mm) with PZT actuator/sensors (thickness = 0.40 mm, diameter = 10.00 mm) has been carried out in ABAQUS implicit (modeling of PZT) and explicit solvers (for SCP) [18]. The explicit and implicit solutions are linked by assigning the 'standard-explicit-co-simulation' [44]. In the SCP (i) and (ii) models, zero-volume (approx.) debond (30×30 mm) regions are modeled by releasing connections between the inter-facial node-to-node connections. The SCPs are modeled with the 8-node brick element ($0.5 \times 0.5 \times 0.2$ mm), 'C3D8I'. These elements offer the advantage of hourglass control, elimination of shear locking and reduced volumetric locking. Each node has 3 degrees-of-freedom (translational). The material properties (homogenised) of quasi-isotropic CFCL are considered based on the empirical formulations in [45] given in Table 1.

The PZTs (actuator and sensors) are modeled using the 8-node C3D8E (standard implicit) linear-piezoelectric brick element ($0.05 \times 0.05 \times 0.1$ mm (approx.)) that supports the behaviour of electromechanical-coupling. The actuation signal (i.e., 150 kHz) is applied (as voltage (V)) to the nodes of the PZT-actuator top-face whereas a 0 V is assigned to the nodes of both sensor and actuator PZTs bottom-face. Output signals of propagating GWs are recorded at the top-face nodes of the PZT sensors: S1, S2, ..., S5 (ref. Fig. 1). The properties of NCE51 PZTs (actuator/sensor) are selected based on the manufacturer (NOLIA[®] Kvistgård, Denmark) and the constitutive equation details are described in [46].

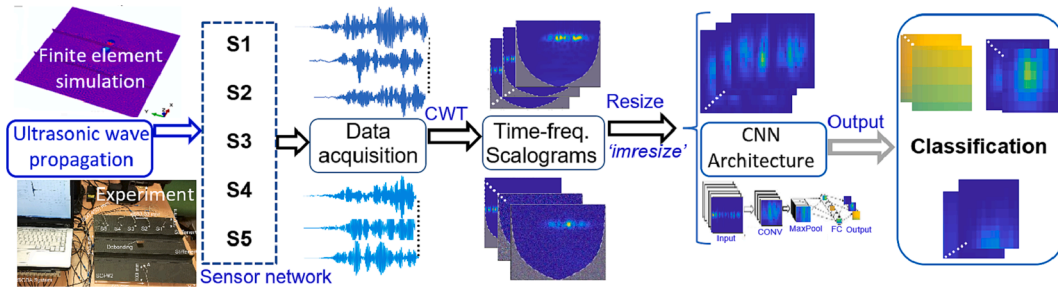


Fig. 4. Schema of the SHM strategy for deep learning-based classification of SCPs.

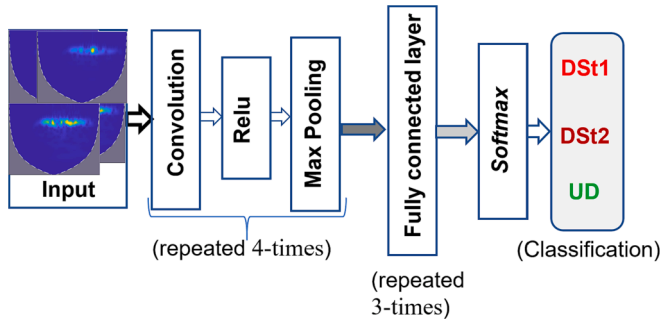


Fig. 5. Designed architecture of the CNN for structural classification.

$$stiffnessconstants : [C] = \begin{bmatrix} 131 & 8.6 & 90.5 & 0 & 0 & 0 \\ 0 & 131 & 90.5 & 0 & 0 & 0 \\ 0 & 0 & 121 & 0 & 0 & 0 \\ 0 & 0 & 0 & 20.11 & 0 & 0 \\ 0 & 0 & 0 & 0 & 20.11 & 0 \\ 0 & 0 & 0 & 0 & 0 & 22.4 \end{bmatrix} [GPa]$$

Mass-density: $\rho = 7200 \text{ [kg/m}^3\text{]}$,

$$permittivity\ constants : [e] = \begin{bmatrix} 1944 & 0 & 0 \\ 0 & 1944 & 0 \\ 0 & 0 & 1911 \end{bmatrix} \times 8.85 \times 10^{-12} [F/m] \text{ and}$$

coupling constants : $[e]$

$$= \begin{bmatrix} 0 & 0 & 0 & 0 & 13.35 & 0 \\ 0 & 0 & 0 & 13.35 & 0 & 0 \\ -6.14 & -6.14 & 15.76 & 0 & 0 & 0 \end{bmatrix} [C/m^2]$$

Three types of SCP models are prepared: (i) undamaged (i.e., UD), (ii) debonds in stiffener#1 (i.e., DSt1), and (iii) debonds in stiffener 2 (i.e., DSt2). The numerical models of the experimental SCP samples are presented in Fig. 3.

In the numerical simulation, 15 DSt1-type SCP models are prepared with a 30 mm DSt1-type debond (ref. Fig. 3(b)) contiguously located along the stiffener#1 length ($15 \times 30 \text{ mm} = 450 \text{ mm}$); 15 DSt2-type SCP models are prepared with a 30 mm baseplate-stiffener#2 debond (ref. Fig. 3(c)) contiguously located along the stiffener#2 length; and 15 UD-type SCP models (ref. Fig. 3(a)) are also prepared with a minutely shifted ($\pm 3 - 5 \text{ mm}$ concerning the experimental ‘A’ position) actuator positions. In the SCP models, the contact acoustic nonlinearity is assigned to the baseplate and stiffener debond surfaces by assigning the *surface-to-surface* frictionless contact to avoid any penetration between the debond region surfaces while applying the wave propagation loading. A direct enforcement formulation that uses the Lagrange multiplier is assigned to maintain the pressure and penetration. The direct enforcement condition for contact virtual work contribution, ‘ $\partial \Pi_{Con}$ ’ is obtained using variational formulation [47] as:

$$\partial \Pi_{Con} = \partial f x + f \partial x \tag{1}$$

where ‘ f ’ represents the contact pressure and ‘ x ’ represents the over-closure. For hard contact, the contact pressure between 2-surfaces at a

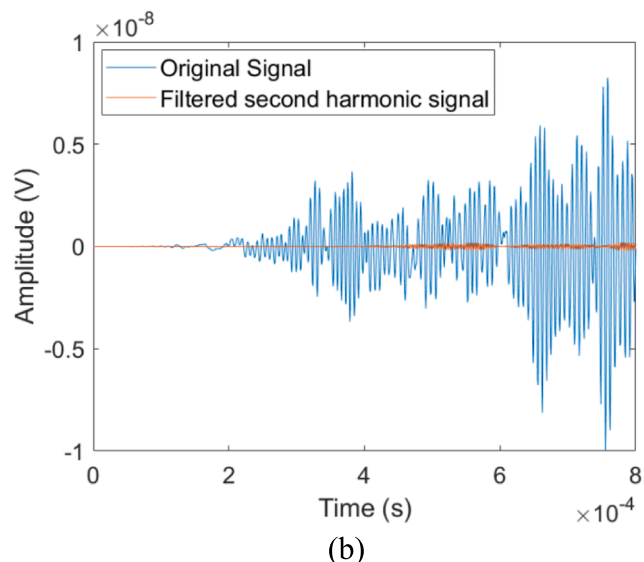
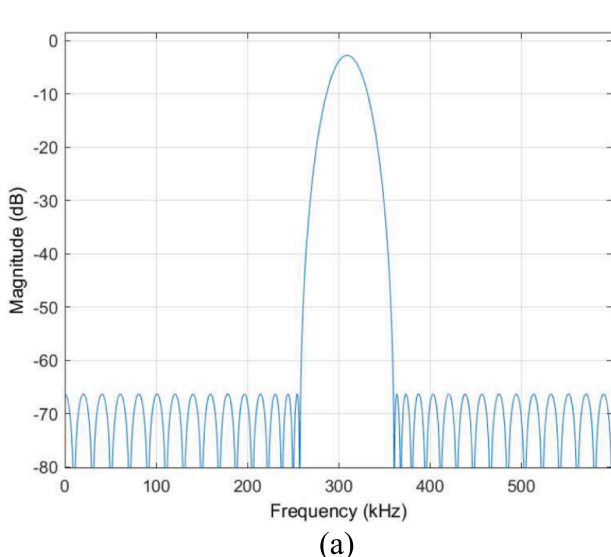


Fig. 6. (a) Frequency-response of the designed filter and (b) an extracted HH1 from raw GWs.

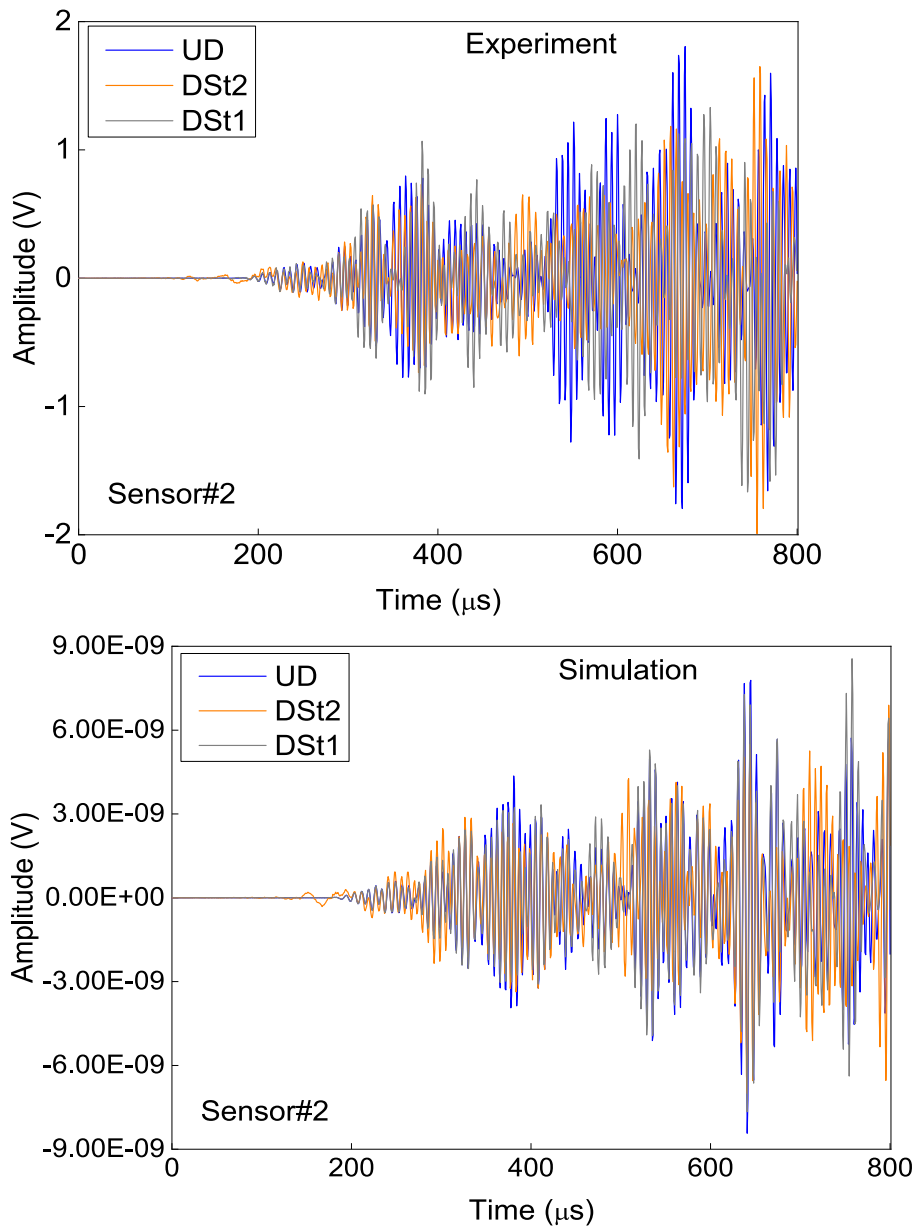


Fig. 7. (a) experiment and (b) simulation signals: healthy, DSt2 and DSt1 debond.

particular point is defined as a function of the overclosure/interpenetration of the surfaces. This contact condition is defined with

$$conditions \left. \begin{matrix} f=0 \text{ when } s < 0 \text{ the surfaces are separating} \\ s=0 \text{ when } f > 0 \text{ the surfaces are contacting} \end{matrix} \right\} 2$$

The Rayleigh damping coefficients of mass proportional and frequency proportional have been considered for the numerical models. A time increment of 5×10^{-8} second/time-step was selected for the implicit and explicit solvers. In all numerical modelling, the actuator PZT ‘A’ generates a 150 kHz 7-cycle sine excitation pulse (Fig. 2(a)) and the ultrasonic GWs are collected at each of the five sensor locations in the PZT network (Fig. 3(a)).

4. SHM strategy based on deep learning

The SHM strategy being presented here uses the GW time-history signals from the sensors and produces time–frequency scalogram images of these time-history signals by applying CWT based on the Morse

Wavelet [48]. CWT is a convolution of the input dataset with a set of functions rendered by the mother wavelet. The convolution can be computed by using an FFT algorithm. Generally, the output is a real-valued function apart from a complex mother wavelet that converts the CWT to a complex function. Generalized Morse wavelets are a family of analytic wavelets [48] of complex values whose Fourier transform is affirmed only along the real axis with positive values. CWT is useful for studying modulated signals with time-varying frequency and amplitude. CWT is also useful for examining localized discontinuities. CWT produces RGB scalograms with its time–frequency spectrums. The extracted features of the dominant frequencies and the related scales from these plots are utilised for training and validation of a signal-classifier of a Neural Network. Here, the generated scalograms as input are supplied to the deep-learning network to train and characterize the 3 different SCP classes: (i) UD, (ii) DSt2, and (iii) DSt1.

Fig. 4 represents a schema of the SHM strategy that uses CNN-based deep learning for the automatic assessment of breathing debonds in

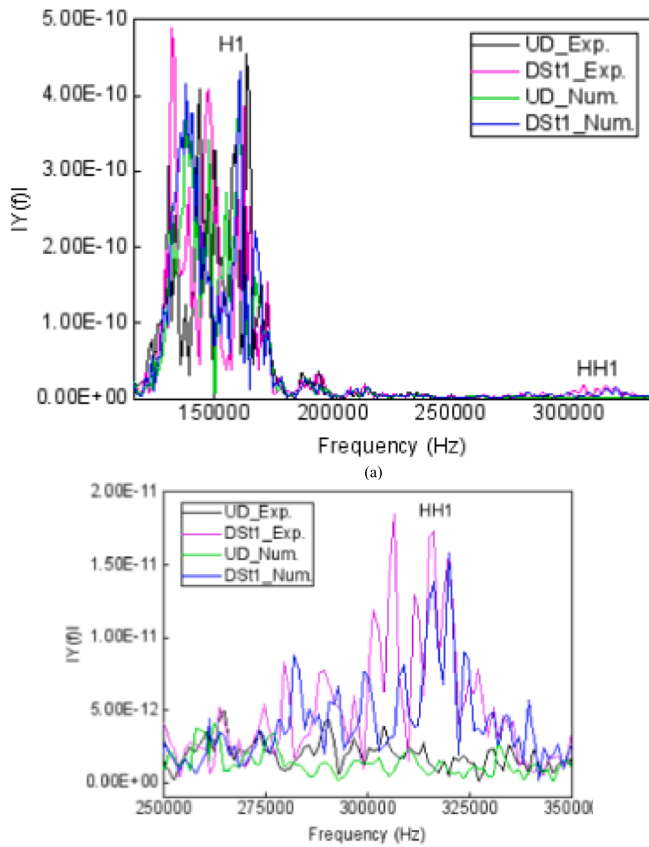


Fig. 8. Healthy and breathing-debond informed (a) raw and (b) HH1 signals (frequency-domain).

SCPs. The training/validation and test process of the designed CNN architecture are described below.

4.1. CNN-based deep learning architecture

A block diagram of the designed CNN consisting of 6 different layers is presented in Fig. 5. The functions of each layer of CNN for the current problem are discussed here in brief. A detailed description is given in [49,50]. In the CNN algorithm, the input scalograms are converted to RGB pixels and supplied to the network. In this current problem, each of the Red, Green and Blue (i.e., RGB) has [292 × 219 pixels] and separate convolution kernels are assigned for each pixel matrix and a bias is added after the convolution. The outputs from these three channels (RGB) are then combined to obtain the output from this layer. A zero padding is assigned after the convolution to avoid any information loss due to the reduction in the successive layers. The value of bias and convolution kernel weights are updated through back-propagation.

In this problem, the convolution kernel size (i.e., filter) is 8*8 pixels and the kernel number is selected as 20 (trial based) to handle valuable information. After the convolution process, an activation function, 'Relu (rectified linear unit)' given in Eq. (3) is applied for mapping all the negative element values to zero.

$$F(y) = \begin{cases} yy \geq 0 \\ 0y < 0 \end{cases} \quad 3$$

RELU is chosen over the 'sigmoid' and 'tanh' functions owing to the higher speed and accuracy [46]. After the RELU operation, a down-sampling is performed by the max-pooling layer to reduce any dimensionality involved in the feature maps. Max-pooling picks max. values of the [2*2] size sliding window. In order to learn large-feature patterns, the selected features from the last layer of max-pooling are compounded

in the fully connected layer (FCL). The classification stage commences from this FCL that multiplies the inputs from the pooling layer by adding a weight matrix and a bias vector. In the current problem, the FCL output size is equal to the dataset class numbers. This deep learning network training is an optimization operation that computes loss-function gradients from every iteration to minimize loss for the assigned training data with updated weight components. The image pixel, weight and bias are the loss function's input. Loss-function considered in here is the 'softmax' that considers the multinomial logistic loss [49]. The posterior probability Q_i of the true class m_i for a feature sample, 'S' is given as

$$u_i = Q_i(m_i|s) = \frac{\exp[a_i^T s + a_{i0}]}{\sum_{j=1}^n \exp[a_j^T s + a_{j0}]} \quad 4$$

where the score vector $u(u_1, u_2, \dots, u_n)$ calculates the proceeding features between 0 and 1 with the sum = 1, a_{i0} is the bias and a_i is the vector of weights that are updated by backpropagation. A loss function, $l(a)$ is defined as:

$$l(a) = -U_g^T \ln(u) \quad 5$$

where $U_g(U_{g1}, U_{g2}, \dots, U_{gm})$ represents the ground-truth vector [49]. The Ground-truth offers checking results corresponding to the real features. The loss function in Eq. (5) estimates the difference between current and targeted models. The value of ground truth (U) for the aimed neurons is 1 whereas for the rest of the neurons is 0, and loss is reduced by updating the 'weights' and the 'bias'. The updated weight values are obtained as:

$$a_{updated} = a_{previous} - R \frac{\delta_l}{\delta a_{previous}} \quad 6$$

where R represents a learning rate (user-defined) which depends on computational time and accuracy in information. A cross-entropy loss, α is estimated by the classification layers with m mutually exclusive classes for multiclass classification. The layer of 'softmax' followed by the classification layer connects the final FCL and the loss function is a cross-entropy of an 1-of- m coding approach. Equation (7) represents the cross-entropy-loss or logarithmic-loss as:

$$\alpha = -\frac{1}{S} \sum_{i=1}^s \sum_{j=1}^m y_{ij} \cdot \log p_{ij} \quad 7$$

where the sample no. is 's', class no. is 'm', p_{ij} represents either 1 pointing whether i^{th} s belongs to the j^{th} m otherwise, it is 0; y_{ij} is the output for i^{th} s and j^{th} m from the layer of 'softmax' [50].

4.2. Higher harmonic extraction from the raw GW signals

The 2nd harmonic signals with a double central frequency (i.e., 300 kHz (approx.)) to the fundamental excitation frequency (i.e., 150 kHz) are extracted from the raw signals by applying a designed filter. The filtered signal consists of debond information, and it is important to maintain the signal's shape while filtering. Hence, an FIR (Finite Impulse Response) filter with a linear phase is chosen to ensure a distortion-free shape without much group delay [51–53]. A bandpass FIR Equiripple filter is designed to separate the 2nd harmonic signals having a peak around 310 kHz. The frequency response of the Equiripple filter is shown in Fig. 6(a) and a typical representation of second harmonic (HH1) the extraction from the raw GWs is given in Fig. 6(b).

5. Results and observations

5.1. Analysis of GW signals from experiment and simulation

GW signals for different cases are obtained from numerical simulations and experiments. The typical experimental GW signals

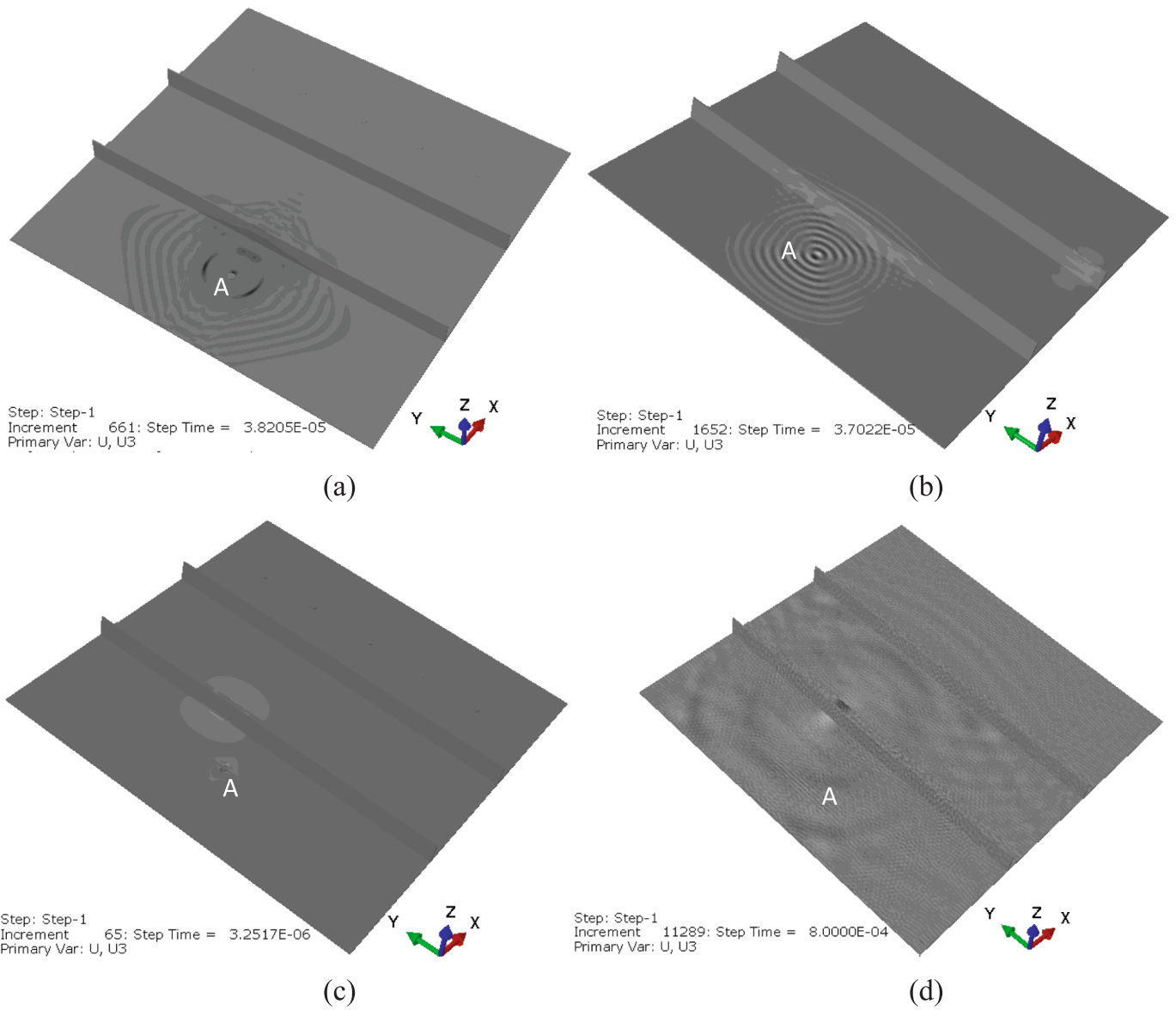


Fig. 9. Waveform plots corresponding to (a) experimental UD case, (b) experimental Dst2 case, (c) experimental Dst1 case and (d) Dst1 case at a later stage where the breathing-debond is acting as the ultrasonic source.

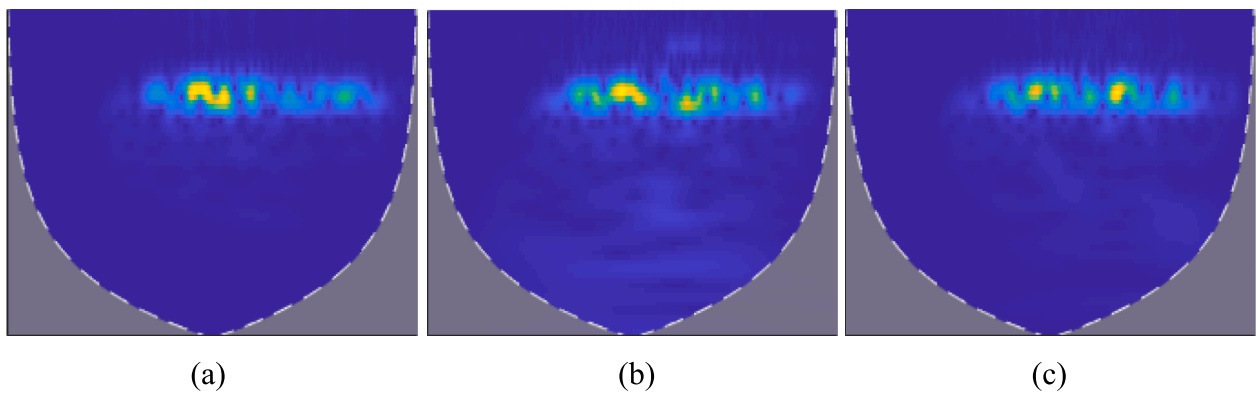


Fig. 10. Reduced CWT scalograms of S4 signals corresponding to (a) UD, (b) Dst1 and (c) Dst2.

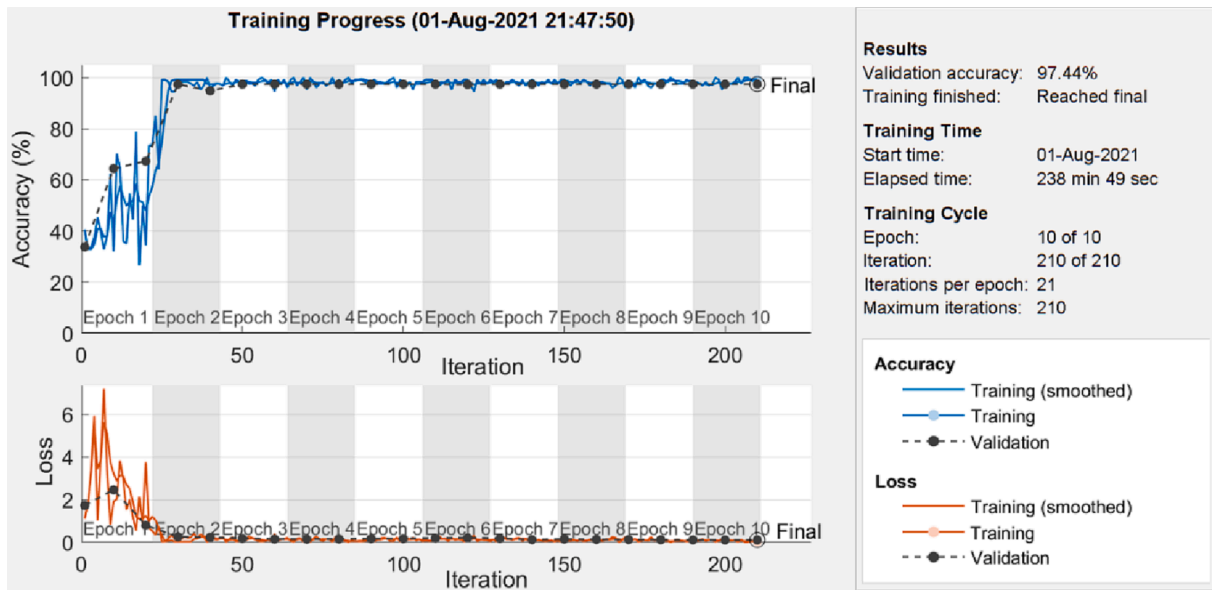
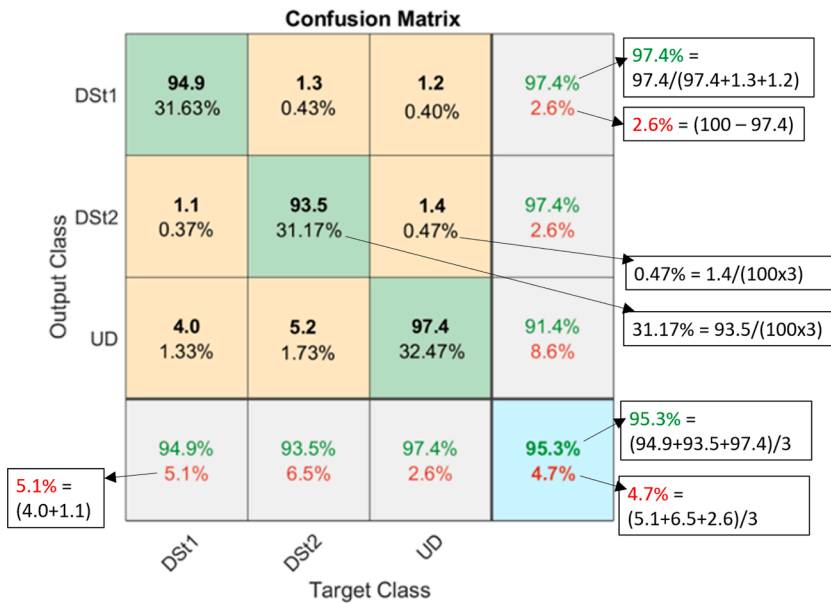


Fig. 11. Training-validation plot represents the loss and accuracy.

Table 2

The confusion matrix shows the 10-fold Av.test performance of the trained network.



corresponding to the undamaged and damaged cases are presented in Fig. 7(a) and the typical numerical signals from undamaged and damaged cases are shown in Fig. 7(b). It is realized that the propagated GWs in SCP at 150 kHz produce multiple GW modes. The frequency–response of the experimental and numerical undamaged and debond influenced signals are presented in Fig. 8(a) that indicating the occurrence of higher harmonics owing to the breathing-like (opening-closing) phenomenon at the region and the presence of second harmonic (HH1) is a prominent for both DSt1 and DSt2 debond cases. Fig. 8(b) shows a clearer pattern of the HH1 signals.

Some typical waveform plots from the numerical SCP models subjected to the Dst2 (ref. Fig. 1), DSt1 and UD are presented in Fig. 9(a)–9 (d), respectively. The waveform plots in Fig. 9 also show the generation and propagation of breathing-debond-induced nonlinear ultrasonic waves (e.g. HH1) in damaged SCPs, due to the breathing of stiffener-baseplate debond. Similar signal characteristics are observed in all

other (DSt1, DSt2 and UD) study cases.

5.2. SHM of SCPs using raw GW signals

The experimental and numerical ultrasonic GW signals (time-domain) are collected from 5 PZT sensors for the debond cases (DSt1 and DSt2) and variable actuator positions for the UD cases. The GW dataset consisted of 3 primary classes – UD, DSt2, DSt1, and two additional test datasets corresponding to (i) 3 experimental analysis cases (UD, DSt1 and DSt2) and (ii) 2 new debond cases (DSt1 and DSt2). In each case, the ultrasonic GW signals are registered from the 5 PZT sensors. These raw time-domain signals for a fixed window size of 800 microseconds are then transformed into time–frequency CWT scalograms, as represented in Fig. 10. Each of the RGB scalogram image sizes is found to be [840 × 630 × 3] (i.e. length × width × channels) pixel.

The scalogram sizes (pixels) are carefully reduced to [292 × 219 × 3

Table 3
Test performance of the trained network for the experimental test dataset.

Confusion Matrix					
Output Class	DSt1	86.4 28.80%	7.0 2.33%	5.2 1.73%	87.6% 12.4%
	DSt2	3.2 1.06%	78.8 26.26%	3.3 1.10%	92.4% 7.6%
	UD	10.4 3.46%	14.2 4.73%	91.5 30.50%	78.8% 21.2%
		86.4% 13.6%	78.8% 21.2%	91.5% 8.5%	85.6% 14.4%
	DSt1	DSt2	UD		Target Class

Table 4
10-fold average test performance of the network for the new datasets.

Confusion Matrix					
Output Class	DSt1	92.2 46.1%	2.4 1.2%	0 0.0%	97.5% 2.5%
	DSt2	3.6 1.8%	93.5 46.75%	0 0.0%	96.3% 3.7%
	UD	4.2 2.1%	4.1 2.05%	0 0.0%	0% 100%
		92.2% 7.8%	93.5% 6.5%	NaN% NaN%	92.85% 14.4%
	DSt1	DSt2	UD		Target Class

pixels] to abridge the computational cost. Farther, the 0-mean Gaussian noise was randomly selected within the range of 10 % to 30 % and added to the resized CWT scalograms for image augmentation as schematically shown in Fig. 4. The Gaussian noise consists of a probability density function resembling a normal distribution and for image augmentation, a random Gaussian function can be added to the image function to introduce this noise. The zero mean value of the noise does not contribute to a net disturbance as the amount of positive and negative noise is the same and ultimately gets cancelled out from the system. A total of 4500 scalograms are obtained and 80 % of the scalograms (i.e.,

3600) are considered for training, 10 % scalograms (i.e., 450) are used for the validation of the network and the remaining 10 % scalograms (i.e., 450) are used for testing of the trained network. The deep learning network described in Section 4 is trained/validated/tested using datasets consisting of the resized scalogram images corresponding to the UD, DSt2 and DSt1 classes. A 10-fold training/validation and test have been conducted to achieve the stable performance of the deep learning network. A total of 4500 images corresponding to the classes: UD, DSt2 and DSt1 are distributed into 10- parts with 450 images/part. Stage 1: part-1 for Testing and part-2...part-10 for Training/Validation. Stage 2: part-1, part-3...part-10 for Training/Validation and part-2 for Testing. Likewise, Stage 3 to Stage 10 have been performed to improve confidence with training progress. The validation accuracy and loss curves have shown some oscillations during the early epochs, due to the usage of limited images per batch. After every passing batch through the CNN, updated weight values are applied with a proportion of all the classes. In order to avoid any overfitting, 10 epochs and 31 iterations/epoch are considered to train the network. A typical training-validation result in Fig. 11 indicates validation accuracy and loss. 10-fold training and validation results show a 97.39 % average (av.) accuracy = $\{(96.84 + 96.98 + 97.16 + 97.22 + 97.64 + 98 + 97.46 + 97.68 + 97.44 + 97.44) / 10\}$. The confusion chart in Table 2 shows the test performance per SCP class with an overall 10-fold average of 95.3 % accuracy.

Further, the trained-network's performance is evaluated for the experimental test datasets corresponding to a UD SCP, an SCP with a DSt2 debond and an SCP with a DSt1 debond. Table 3 confusion matrix shows an overall 85.6 % test accuracy (10-fold av.) for the experimental data.

The deep learning model was trained with the simulation dataset and the test performance with available experimental data (never used for training) produced high accuracy justifies the SHM potential of the proposed deep-SHM model and the simulation success. The trained network is then tested for 2 entirely new debond datasets corresponding to a DSt1 and a DSt2 debond. The 10-fold average accuracy (92.85 %) in Table 4 indicates the robustness of the deep learning architecture for breathing-debond monitoring. The NaN% resembles zero input in the UD channel.

5.3. SHM of SCPs using filtered HH1 signals

The designed neural network is trained with time-frequency scalograms of HH1 (260 – 360 kHz) that are extracted from the raw ultrasonic signals (ref. Fig. 6) by using the designed bandpass filter described in sub-section 4.2. Fig. 12 (a) represents a typical time-history signal of extracted HH1 and its resized time-frequency scalogram image is presented in Fig. 12 (b).

The tenfold training, validation and test are performed with HH1-signal datasets and a training/validation performance (i.e., 1 of 10 results) of the network is presented in Fig. 13 and shows a very high accuracy (99 %). Whereas the 10-fold av. training-validation accuracy was found to be 98.99 % = $\{(98.64 + 98.8 + 98.98 + 99.11 + 99.14 + 99.00 + 99.00 + 99.12 + 99.14 + 99.00)/10\}$. This accuracy is significantly better than the results using the raw GW dataset. Further, the 10-fold training-validation with the raw data and the HH1 data are compared and represented in Fig. 14 indicating a better accuracy for the extracted HH1signals than the raw data.

The 10-fold training-validation accuracy corresponding to the raw data standard deviation (SD_{RD}) and HH1 data standard deviation (SD_{HH1}) of the was calculated as:

$$SD_{RD} = \sqrt{\frac{\sum (x_i - \mu)^2}{n}} = 0.328761312$$

$$SD_{HH1} = \sqrt{\frac{\sum (x'_i - \mu')^2}{n}} = 0.484984536$$

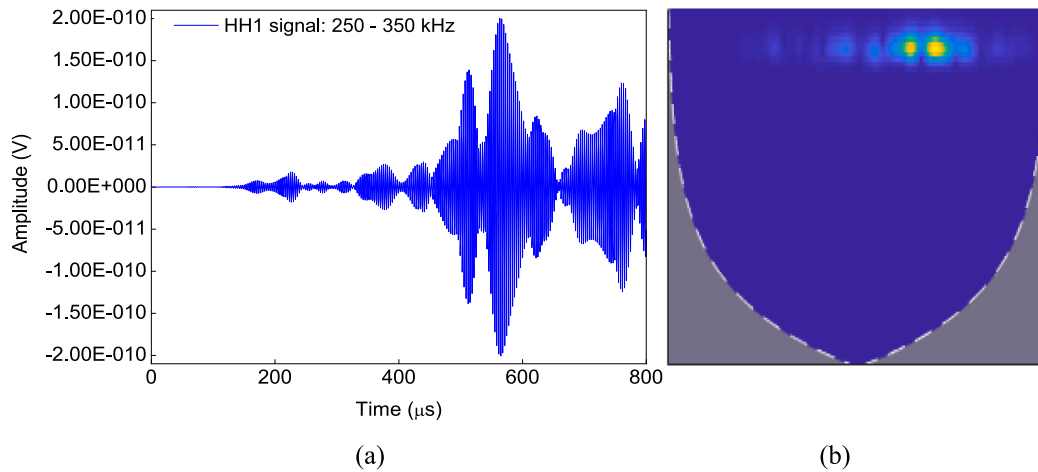


Fig. 12. Typical (a) HH1signal (time-history) and (b) its CWT scalogram (time–frequency).

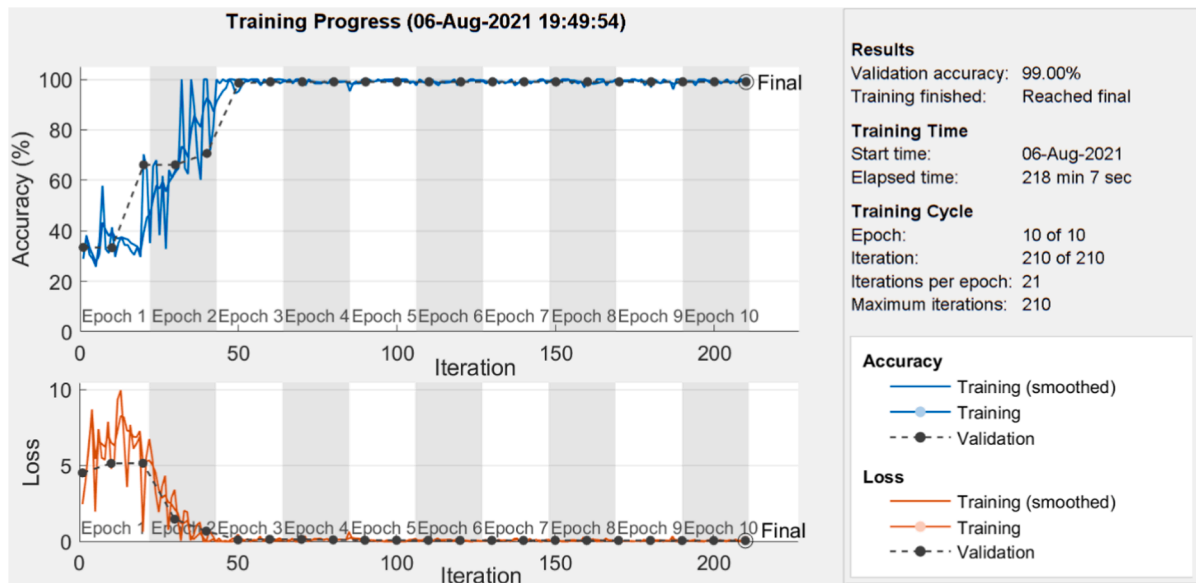


Fig. 13. Training and validation performance of the deep learning network with HH1 data.

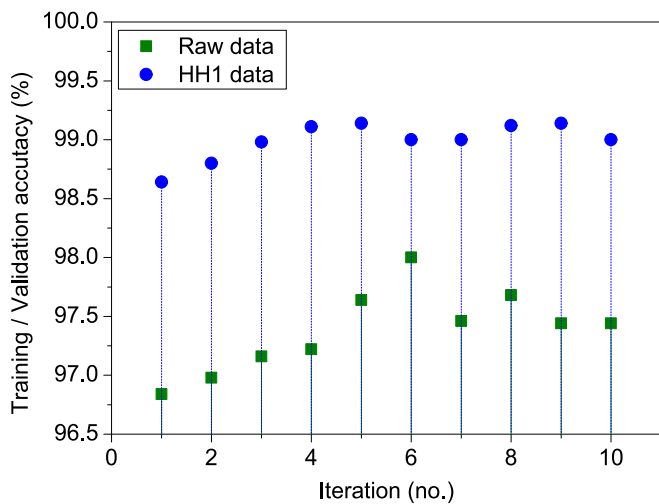


Fig. 14. 10-fold training/validation performance using raw data and HH1.

where ‘ x_i ’ is the 10-fold training-validation accuracy using raw data = [96.84, 96.98, 97.16, 97.22, 97.64, 98, 97.46, 97.68, 97.44, 97.44]; ‘ μ ’ is the mean accuracy using raw data = 97.386; ‘ x_i ’ is the 10-fold training-validation accuracy using HH1 data = [98.64, 98.8, 98.98, 99.11, 99.14, 99.00, 99.00, 99.12, 99.14, 99.00]; ‘ μ ’ is the mean accuracy using HH1 data = 98.993 and ‘ n ’ is number of trials = 10.

Table 5 confusion chart represents the 10-fold average test performance (97.3 % accuracy) of the trained networks using only 100 RGB scalograms per class. Fig. 15 shows a comparison between the test performance using raw data (ref. Table 2) and the extracted HH1 signal data (ref. Table 5). The HH1 signal data-based results show better accuracy than the raw signal data-based results for each of the SCP classes.

The damage region classification potential of the network is evaluated for the experimental HH1 scalograms corresponding to the UD, DSt1 and DSt2. The test results in Table 6 confusion matrix show the overall accuracy of 90.4 % of the network, which is again more than the raw GW data-based test results (i.e. 85.6 %).

Further, a class-wise comparison between the experimental raw and HH1 data-based test performance is presented in Fig. 16. The comparison shows higher test accuracies for the HH1 data-based results, in all the SCP classes.

Table 5
10-fold average test performance using the HH1.

		Confusion Matrix			
Output Class	DSt1	96.8 32.27%	1.9 0.63%	0.8 0.27%	97.3% 2.7%
	DSt2	1.4 0.47%	96.5 32.17%	0.5 0.17%	98.1% 1.9%
	UD	1.8 0.60%	1.6 0.53%	98.7 32.90%	96.7% 3.3%
		96.8% 3.2%	96.5% 3.5%	98.7% 1.3%	97.3% 2.7%
		Target Class			
		DSt1	DSt2	UD	

Table 6
The average test performance using the experimental HH1 signals.

		Confusion Matrix			
Output Class	DSt1	89.6 29.87%	5.3 1.77%	4.1 1.37%	90.5% 9.5%
	DSt2	3.3 1.1%	88.3 29.43%	2.5 0.83%	93.8% 6.2%
	UD	7.1 2.36%	6.4 2.13%	93.4 31.13%	87.4% 12.6%
		89.6% 10.4%	88.3% 21.2%	93.4% 8.5%	90.4% 9.6%
		Target Class			
		DSt1	DSt2	UD	

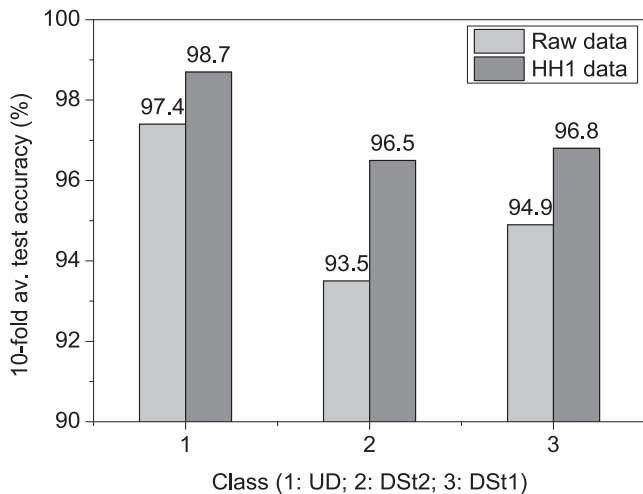


Fig. 15. Class-wise 10-fold average test performance corresponding to raw and HH1 signals.

The SHM potential of the designed neural network is further evaluated for the HH1 signals from DSt1 and DSt2 datasets (never used for training). The 10-fold average test performance in Table 7 shows an overall 95.9 % accuracy, resembling the robustness of the SHM strategy. The NaN% has again appeared in the confusion matrix owing to the no input in the UD channel.

Fig. 17 represents a class-wise comparison between the HH1 signal and raw-GW image-based test results (10-fold av.) for DSt1 and DSt2 that again proves the better performance for the extracted higher-harmonic signals, in both the classes.

6. Conclusions

A deep learning based SHM strategy is presented for the assessment of SCPs using nonlinear ultrasonic signals. This study is amongst the first to propose a damage identification methodology using a deep learning

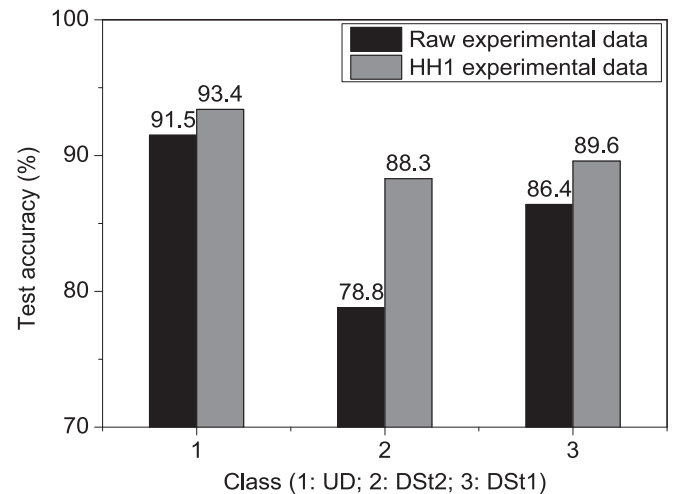


Fig. 16. 10-fold average test performance per class using raw data and HH1 data.

approach for complex stiffened composite panels with nonlinear ultrasonic signals. The SHM strategy has the advantage of being physics-informed and data-driven by experimental guided wave data. This work has proven the potential of the deep learning-based SHM strategy for classifying breathing-debond regions in stiffened composite structures. This monitoring strategy provides the foundation for an automated strategy for the extraction of essential signal features (filtering and transformation) to be incorporated into the deep learning models. Thus, the potential of the proposed methodology can be explored for the assessment of a wide range of damages with acoustic fingerprints recorded at the sensory network and the trained model can be deployed for real-time or online identification of damages for operational complex lightweight structures.

The main conclusions can be listed as follows.

Table 7
Test performance (10-fold av.) with HH1 data from the new debond.

		Confusion Matrix			
Output Class		Dst1	Dst2	UD	
		Dst1	95.5 47.75%	1.2 0.60%	0 0.0%
Dst2	1.3 0.65%	96.3 48.15%	0 0.0%	98.7% 1.3%	
UD	3.2 1.6%	2.5 1.25%	0 0.0%	0% 100%	
		95.5% 4.5%	96.3% 3.7%	NaN% NaN%	95.9% 4.1%
		Dst1	Dst2	UD	
		Target Class			

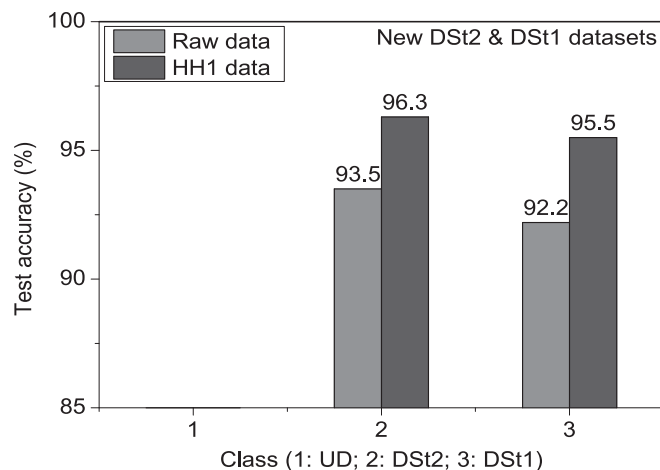


Fig. 17. 10-fold av. test results for new Dst1 and Dst2 cases with raw data and their HH1 data.

- In the given study conditions (e.g., SCP geometry, loading), the breathing-debond-induced nonlinear ultrasonic signals show a prominent HH1 signature in the registered GW signals. The existence of any other higher-harmonics or sub-harmonics is not recognized.
- The test confusion charts of the trained deep learning network prove that the SHM strategy can effectively classify the 3-primary classes (i.e. UD, Dst2, Dst1) of the SCPs with high precision using the experimental untrained datasets and with the datasets from new debonds.
- This network can offer an improved training/validation/test performance with the filtered second harmonic (HH1) signals than the raw GWs.
- The average (10-fold) test performance of the raw and the HH1 datasets confirms that the proposed SHM strategy is more impactful with the HH1 datasets.

It is envisaged that this research will contribute to the development

of industry-grade autonomous damage identification toolbox in the near future. This will be especially applicable for the identification of structural damages which have nonlinear ultrasonic signatures and can facilitate the prevention of catastrophic damages resulting from large relative motions between damaged structural components. The future research direction will be focused on the characterisation of various types of damages in composites, especially involving the following-

- the influence of damage size, severity and damage types (e.g., delamination, crack) on GW signal characteristics.
- exploring the scope of applying unsupervised learning methods (e.g., hierarchical clustering) for outlier identification and damage classification related to the events of nonlinear ultrasonics
- uncertainty quantification and management to account for the influences on identified damage metrics due to variable loading and operating cases.

These continue to be part of the ongoing research work by the authors.

CRediT authorship contribution statement

Shirsendu Sikdar: Conceptualization, Data curation, Formal analysis, Investigation, Methodology, Validation, Visualization, Writing – original draft, Writing – review & editing, Funding acquisition, Project administration, Resources. **Wiesław Ostachowicz:** Visualization, Writing – review & editing, Funding acquisition, Project administration, Resources. **Abhishek Kundu:** Visualization, Writing – review & editing, Funding acquisition, Resources.

Declaration of Competing Interest

The authors declare that they have no known competing financial interests or personal relationships that could have appeared to influence the work reported in this paper.

Data availability

Data will be made available on request.

Acknowledgement

This research was supported by Physical Research Council (EPSRC) in the UK under grant agreement number EP/V055577/1 and Polish National Science Centre (NCN) in Poland under grant number UMO-2018/29/B/ST8/02904.

References

- [1] Matthews FL, Rawlings RD. Composite materials: engineering and science. Elsevier; 1999.
- [2] Eaton MJ, Pullin R, Holford KM. Acoustic emission source location in composite materials using Delta T Mapping. *Compos A Appl Sci Manuf* 2012 Jun 1;43(6): 856–63.
- [3] Safri SN, Sultan MT, Jawaid M, Jayakrishna K. Impact behaviour of hybrid composites for structural applications: a review. *Compos B Eng* 2017;133:112–21.
- [4] Sha G, Radzienski M, Soman R, Cao M, Ostachowicz W, Xu W. Multiple damage detection in laminated composite beams by data fusion of Teager energy operator-wavelet transform mode shapes. *Compos Struct* 2020 Mar;1(235):111798.
- [5] Bogenfeld R, Kreikemeier J, Wille T. An analytical scaling approach for low-velocity impact on composite structures. *Compos Struct* 2018;187:71–84.
- [6] Koh TM, Isa MD, Feih S, Mouritz AP. Experimental assessment of the damage tolerance of z-pinned T-stiffened composite panels. *Compos B Eng* 2013;44(1): 620–7.
- [7] Shroff S, Acar E, Kassapoglou C. Design, analysis, fabrication, and testing of composite grid-stiffened panels for aircraft structures. *Thin-Walled Struct* 2017 Oct;1(119):235–46.
- [8] Zheng K, Li Z, Ma Z, Chen J, Zhou J, Su X. Damage detection method based on Lamb waves for stiffened composite panels. *Compos Struct* 2019 Oct;1(225): 111137.

- [9] Soleimanpour R, Ng CT. Locating delaminations in laminated composite beams using nonlinear guided waves. *Eng Struct* 2017 Jan;15(131):207–19.
- [10] Li Z, Zhou L, Lei H, Pei Y. Microwave near-field and far-field imaging of composite plate with hat stiffeners. *Compos B Eng* 2019 Mar;15(161):87–95.
- [11] Yetman JE, Sobey AJ, Blake JJ, Shenoi RA. Investigation into skin stiffener debonding of top-hat stiffened composite structures. *Compos Struct* 2015 Nov;15(132):1168–81.
- [12] Sha G, Xu H, Radziński M, Cao M, Ostachowicz W, Su Z. Guided wavefield curvature imaging of invisible damage in composite structures. *Mech Syst Sig Process* 2021 Mar;1(150):107240.
- [13] Su Z, Ye L, Lu Y. Guided Lamb waves for identification of damage in composite structures: a review. *J Sound Vib* 2006 Aug 22;295(3–5):753–80.
- [14] Sikdar S, Fiborek P, Kudela P, Banerjee S, Ostachowicz W. Effects of debonding on Lamb wave propagation in a bonded composite structure under variable temperature conditions. *Smart Mater Struct* 2018 Nov;28(1):015021.
- [15] Kundu T. Fundamentals and Applications of Nonlinear Ultrasonic Nondestructive Evaluation. In: *Ultrasonic and Electromagnetic NDE for Structure and Material Characterization* 2016 Apr 19 (pp. 410–471). CRC Press.
- [16] De Luca A, Perfetto D, Lamanna G, Aversano A, Caputo F. Numerical investigation on guided waves dispersion and scattering phenomena in stiffened panels. *Materials* 2021 Dec 23;15(1):74.
- [17] Memmolo V, Monaco E, Boffa ND, Maio L, Ricci F. Guided wave propagation and scattering for structural health monitoring of stiffened composites. *Compos Struct* 2018 Jan;15(184):568–80.
- [18] Ciampa F, Pickering SG, Scarselli G, Meo M. Nonlinear imaging of damage in composite structures using sparse ultrasonic sensor arrays. *Struct Control Health Monit* 2017 May;24(5):e1911.
- [19] Ciampa F, Meo M. Nonlinear elastic imaging using reciprocal time reversal and third order symmetry analysis. *J Acoust Soc Am* 2012;131(6):4316–23.
- [20] Kundu T, editor. *Nonlinear ultrasonic and vibro-acoustical techniques for nondestructive evaluation*. Springer; 2018 Oct 19.
- [21] Chillara VK, Lissenden CJ. Review of nonlinear ultrasonic guided wave nondestructive evaluation: theory, numerics, and experiments. *Opt Eng* 2015 Aug; 55(1):011002 [20] Dong J, Kim B, Loquet.
- [22] Sikdar S, Van Paeppegem W, Ostachowicz W, Kersemans M. Nonlinear elastic wave propagation and breathing-debond identification in a smart composite structure. *Compos B Eng* 2020 Nov;1(200):108304.
- [23] Zhao J, Chillara VK, Ren B, Cho H, Qiu J, Lissenden CJ. Second harmonic generation in composites: theoretical and numerical analyses. *J Appl Phys* 2016 Feb;119(6):064902.
- [24] Matlack KH, Kim JY, Jacobs LJ, Qu J. Review of second harmonic generation measurement techniques for material state determination in metals. *J Nondestruct Eval* 2015 Mar 1;34(1):273.
- [25] Solodov I, Wackerl J, Pfeleiderer K, Busse G. Nonlinear self-modulation and subharmonic acoustic spectroscopy for damage detection and location. *Appl Phys Lett* 2004 Jun 28;84(26):5386–8.
- [26] Lim HJ, Sohn H. Fatigue crack detection using structural nonlinearity reflected on linear ultrasonic features. *J Appl Phys* 2015 Dec 28;118(24):244902.
- [27] Van Den Abeele KA, Carmeliet J, Ten Cate JA, Johnson PA. Nonlinear elastic wave spectroscopy (NEWS) techniques to discern material damage, Part II: single-mode nonlinear resonance acoustic spectroscopy. *J Res Nondestructive Evaluation* 2000 Jan 1;12(1):31–42.
- [28] Yang Y, Ng CT, Kotousov A, Sohn H, Lim HJ. Second harmonic generation at fatigue cracks by low-frequency Lamb waves: Experimental and numerical studies. *Mech Syst Sig Process* 2018 Jan;15(99):760–73.
- [29] Jhang KY. Nonlinear ultrasonic techniques for nondestructive assessment of micro damage in material: a review. *Int J Precis Eng Manuf* 2009 Jan 1;10(1):123–35.
- [30] Seo H, Pyun DK, Jhang KY. Synthetic aperture imaging of contact acoustic nonlinearity to visualize the closing interfaces using tone-burst ultrasonic waves. *Mech Syst Sig Process* 2019 Jun;15(125):257–74.
- [31] He Y, Xiao Y, Su Z, Pan Y, Zhang Z. Contact acoustic nonlinearity effect on the vibro-acoustic modulation of delaminated composite structures. *Mech Syst Sig Process* 2022 Jan;15(163):108161.
- [32] Huang L, Zeng L, Lin J, Zhang N. Baseline-free damage detection in composite plates using edge-reflected Lamb waves. *Compos Struct* 2020;112423.
- [33] Liu P, Sohn H, Park B. Baseline-free damage visualization using noncontact laser nonlinear ultrasonics and state space geometrical changes. *Smart Matererials and Struct* 2015;24(6):065036.
- [34] Avci O, Abdeljaber O, Kiranyaz S, Hussein M, Gabbouj M, Inman DJ. A review of vibration-based damage detection in civil structures: From traditional methods to Machine Learning and Deep Learning applications. *Mech Syst Sig Process* 2021 Jan;15(147):107077.
- [35] Liu H, Zhang Y. Image-driven structural steel damage condition assessment method using deep learning algorithm. *Measurement* 2019 Feb;1(133):168–81.
- [36] Kundu A, Sikdar S, Eaton M, Navaratne R. A Generic Framework for Application of Machine Learning in Acoustic Emission-Based Damage Identification. In: *Proceedings of the 13th International Conference on Damage Assessment of Structures 2020* (pp. 244–262). Springer, Singapore.
- [37] Ewald V, Venkat RS, Asokkumar A, Benedictus R, Boller C, Groves RM. Perception modelling by invariant representation of deep learning for automated structural diagnostic in aircraft maintenance: a study case using DeepSHM. *Mech Syst Sig Process* 2021;108153.
- [38] Sikdar S, Pal J. Bag of visual words based machine learning framework for disbond characterisation in composite sandwich structures using guided waves. *Smart Mater Struct* 2021 May 31;30(7):075016.
- [39] Alvarez-Montoya J, Carvajal-Castrillón A, Sierra-Pérez J. In-flight and wireless damage detection in a UAV composite wing using fiber optic sensors and strain field pattern recognition. *Mech Syst Sig Process* 2020;136:106526.
- [40] Ewald V, Goby X, Jansen H, Groves RM, Benedictus R. Incorporating Inductive Bias into Deep Learning: A Perspective from Automated Visual Inspection in Aircraft Maintenance. In: *Proc. 10th Intl Symposium on NDT in Aerospace*, Dresden 2018 (pp. 1–9).
- [41] Ewald V, Groves RM, Benedictus R. DeepSHM: a deep learning approach for structural health monitoring based on guided Lamb wave technique. In: *Sensors and Smart Structures Technologies for Civil, Mechanical, and Aerospace Systems 2019* Mar 27 (Vol. 10970, p. 109700H). International Society for Optics and Photonics.
- [42] Khan A, Raouf I, Noh YR, Lee D, Sohn JW, Kim HS. Autonomous assessment of delamination in laminated composites using deep learning and data augmentation. *Compos Struct* 2022 Jun;15(290):115502.
- [43] Wu J, Xu X, Liu C, Deng C, Shao X. Lamb wave-based damage detection of composite structures using deep convolutional neural network and continuous wavelet transform. *Compos Struct* 2021 Nov;15(276):114590.
- [44] Abaqus Theory Manual. 2014. Version 6.14-1. Dassault Systemes.
- [45] Vinson JR, Sierakowski RL. *The behavior of structures composed of composite materials*. Springer; 2006.
- [46] Deraemaeker A, Nasser H, Benjeddou A, et al. Mixing rules for the piezoelectric properties of macro fiber composites. *J Intell Mater Syst Struct* 2009;20:1475–82.
- [47] Solodov IY, Krohn N, Busse G. CAN: an example of nonclassical acoustic nonlinearity in solids. *Ultrasonics* 2002;40:621–5.
- [48] Wachowiak MP, Wachowiak-Smolfková R, Johnson MJ, Hay DC, Power KE, Williams-Bell FM. Quantitative feature analysis of continuous analytic wavelet transforms of electrocardiography and electromyography. *Philos Trans R Soc A Math Phys Eng Sci* 2018 Aug 13;376(2126):20170250.
- [49] Huang X, Liu Z, Zhang X, Kang J, Zhang M, Guo Y. Surface damage detection for steel wire ropes using deep learning and computer vision techniques. *Measurement* 2020;161:107843.
- [50] Yamashita R, Nishio M, Do RK, Togashi K. Convolutional neural networks: an overview and application in radiology. *Insights into imaging* 2018 Aug 1;9(4): 611–29.
- [51] Oppenheim AV, Willsky AS, Ian T, *Signals and Systems*, Prentice-Hall, New Jersey, 1982.
- [52] Lutovac MD, Tošić DV, Evans BL. Filter design for signal processing using MATLAB and Mathematica. Miroslav Lutovac 2001.
- [53] Ciampa F, Meo M. Nonlinear elastic imaging using reciprocal time reversal and third order symmetry analysis. *J Acoust Soc Am* 2012 Jun;131(6):4316–23.